

Effect of radius of gyration on a wing rotating at low Reynolds number: A computational study

Daniel Tudball Smith,^{1,*} Donald Rockwell,² John Sheridan,¹ and Mark Thompson¹

¹*Fluids Laboratory for Aeronautical and Industrial Research, FLAIR, Department of Mechanical and Aerospace Engineering, Monash University, Clayton, Victoria 3800, Australia*

²*Department of Mechanical Engineering, Lehigh University, Bethlehem, Pennsylvania 18015, USA*

(Received 21 September 2016; published 5 June 2017)

This computational study analyzes the effect of variation of the radius of gyration (r_g), expressed as the Rossby number $Ro = r_g/C$, with C the chord, on the aerodynamics of a rotating wing at a Reynolds number of 1400. The wing is represented as an aspect-ratio-unity rectangular flat plate aligned at 45° . This plate is accelerated near impulsively to a constant rotational velocity and the flow is allowed to develop. Flow structures are analyzed and force coefficients evaluated. Trends in velocity field degradation with increasing Ro are consistent with previous experimental studies. At low Ro the flow structure generated initially is mostly retained with a strong laminar leading-edge vortex (LEV) and tip vortex (TV). As both Ro and travel distance increase, the flow structure degrades such that at high Ro it begins to resemble that of a translating wing. Additionally, the present study has shown the following. (i) At low Ro the LEV and TV structure is laminar and steady; as Ro increases this structure breaks down, and the location at which it breaks down shifts closer to the wing root. (ii) For moderate Ro of 1.4 and higher, the LEV is no longer steady but enters a shedding regime fed by the leading-edge shear layer. (iii) At the lowest Ro of 0.7 the lift force rises during start-up and then stabilizes, consistent with the flow structure being retained, while for higher Ro a force peak occurs after the initial acceleration is complete, followed by a reduction in lift which appears to correspond to shedding of excess leading-edge vorticity generated during start-up. (iv) All rotating wings produced greater lift than a translating wing, this increase varied from $\sim 65\%$ at the lowest $Ro = 0.7$ down to $\sim 5\%$ for the highest Ro examined of 9.1.

DOI: [10.1103/PhysRevFluids.2.064701](https://doi.org/10.1103/PhysRevFluids.2.064701)

I. INTRODUCTION

In recent years, a rapid increase in research has resulted in increased understanding of low-Reynolds-number flight. Both the development of unmanned microaerial vehicles and advancement of computational and experimental techniques have driven this increased understanding. The incredible performance of natural flyers at these smaller scales has pushed the study of flapping flight to the forefront of many of these investigations. Extensive reviews of flapping and biologically inspired flight have been given by researchers such as Ellington [1], Sane [2], Dickinson [3], Wang [4], and Shyy *et al.* [5]. In the context of the present study, Wolfinger and Rockwell [6] provide a recent review of investigations pertaining to rotational effects on wing performance.

The study presented herein investigates how the flow structures and performance of a rotating wing develop and change with time by varying the contribution from rotational effects compared to translational effects. This variation is achieved by analyzing an aspect-ratio-unity wing of fixed planform and varying the radius of gyration (r_g); that is, moving the wing closer to or further away from the rotation axis. This has practical consequences for flapping unmanned aerial vehicle design, where it is important to understand the effect of increasing rotational effects by shifting the rotation axis. A better understanding of these circumstances is potentially important in effecting better

*daniel.tudball-smith@monash.edu

designs of biomimetic flapping mechanisms as it would affect the design of the drive mechanism for a low-Reynolds-number flyer. For a wing rotating in a flow with no freestream velocity, representative of a hovering flyer, the ratio of rotational effects to translational effects can be described by the Rossby number, which for this case can be expressed as $Ro = r/C$, where r is the characteristic radius and C is the chord length [7]. This study therefore investigates the effect of Rossby number through changes in radius of gyration, noting r_g can be used as the characteristic length such that $Ro = r_g/C$.

An understanding of rotating and flapping wings has been pursued in recent decades and substantial advances have been made. A number of researchers have sought to relate aerodynamic performance to the wing kinematics of various flapping flyers [8,9]. Ellington *et al.* [10] employed qualitative flow visualization to characterize the flow structure along the wings of both live insects and mechanical models, identifying the characteristic stably attached leading-edge vortex (LEV) of a rotating wing. Other researchers have employed quantitative flow visualization to characterize the flow structure along the wings of live insects [11] and also dynamically scaled models [12–14]. Forces on flapping wings have been measured by Lentink and Dickinson [7], Dickinson *et al.* [15], Birch and Dickinson [12], and Poelma *et al.* [13]. These have been supplemented by computational studies on flapping wings [16–20].

Studies such as Ellington [8] and Dickinson *et al.* [15] have suggested that flapping flight can be generalized through several dynamic mechanisms: delayed stall as the wing sweeps through its stroke, additional circulation generated by wing pitch variation during pronation and supination, and wake capture.

Though the full kinematics of natural flyers is complex and varies from one species to the next with great variation in the kinematics and wing geometries, a rotating wing that is accelerated impulsively to a constant rotation velocity is a common simplification used to analyze high lift mechanisms in the middle portion of a wing stroke. Existing research has shown that this simplification of the kinematics gives a good approximation of a downstroke in typical flapping flight and that high lift mechanisms associated with flapping flyers also exist for this simplified case (e.g., [7,13], and various others). The existence of a stable and attached LEV on a rotating wing has been identified in many studies for a range of Reynolds numbers and wing geometries [7,13,21–29]). This stable low-pressure LEV is key to the high performance of rotating wings, as it reattaches the flow separating from the leading edge at high angles of attack that would otherwise cause a translating wing to stall [7,10,25,28]. Recent studies have investigated the effects of low-aspect-ratio wings undergoing rotating and pitching [30–32] and rotating wings undergoing acceleration (surging) [30].

Various researchers have investigated the mechanisms responsible for a stable and attached LEV. Lentink and Dickinson [33] proposed, using an analytical approach, that centripetal and Coriolis forces, when observing the wing in a fixed reference frame, stabilize flow structures compared to a translating wing. Numerical simulations [28,29] have demonstrated Coriolis forces on a fluid element are small compared to forces due to pressure gradients, while centrifugal and pressure gradient forces are responsible for spanwise flow and are important in retaining LEV attachment. Jardin and David’s [34] numerical study supported that of Lentink and Dickinson [33], where centrifugal and Coriolis terms were introduced into simulations independently and it was found that Coriolis effects have a key role to play in lift generation while the impact of centrifugal terms is only marginal. Jardin and David [35] compared the flow over a translating wing in uniform flow, a translating wing with a spanwise velocity gradient as would be seen on a rotating wing, and a purely rotating wing. They found that the spanwise velocity gradient alone does not promote significant lift improvements like a rotating wing does, further emphasizing the importance of forces arising from a rotating reference frame. Additionally, Wojcik and Buchholz [36] proposed that vorticity annihilation due to a layer of opposite-signed vorticity on the plate surface was often a dominant mechanism for regulating the LEV. Recently, Limacher *et al.* [37] identified that Coriolis accelerations limit the spanwise extent of a stable LEV by tilting the LEV core towards the wake. If the average trajectory of the LEV is outwards (towards the tip) and away from the leading edge (towards the wake), then it follows that the corresponding average Coriolis force components will be towards the wake and towards the root, respectively.

Experimental studies [26,38–42] and numerical studies [22,27,29] have further investigated aspect-ratio effects of rotating wings. Harbig *et al.* [27] performed a numerical study on a scaled fruit-fly wing of varying aspect ratio and proposed scaling by a Reynolds number based on the wing's span rather than its chord to decouple Reynolds number and aspect-ratio effects. This is further supported by Carr *et al.* [39]. Fu *et al.* [40] varied aspect ratio and found Kelvin-Helmholtz instabilities in the LEV and vortex bursting at outer spanwise locations for higher aspect ratios. Kruyt *et al.* [41] showed that the leading-edge vortex of a rotating wing of high aspect ratio at high angle of attack remains attached closer to the root and separates beyond four chord lengths of radial distance. Phillips *et al.* [42] estimated lift coefficients from LEV circulation, while Harbig *et al.* [27] estimated lift from numerical simulations. Both found that an increase in aspect ratio initially increases the coefficient of lift and then decreases it at higher aspect ratios ($AR \gtrsim 5$). Each of these aspect-ratio studies show degrading flow structure further from the rotation axis (more distant spanwise locations) for higher aspect ratios.

Wing performance has been linked with rotational effects, with qualitative and quantitative flow visualization showing the difference between a wing rotating with $Ro = O(1)$ (dominated by rotational effects) and rectilinearly translating ($Ro \rightarrow \infty$) [7,24,25,28]. As Rossby number is increased the wing's performance reduces [7,43]; this reduction in performance continues until the wing is in pure translation.

Wolfinger and Rockwell [6] provide a study of Rossby number effects for a fixed aspect-ratio wing where Ro is varied by changing r_g . With flow field reconstructions using stereo particle-image velocimetry (SPIV), it shows that structures attributed to good performance, such as a strong leading-edge vortex pinned to the wing and a large downwash component, are present on wings at low Rossby numbers but degrade as the Rossby number increases. Wolfinger and Rockwell [6] also shows on a rectangular $AR = 1$ wing for small travel distances at high Rossby numbers that the flow structure can be initially favorable but deteriorates the further the wing travels. Therefore for low Rossby numbers, the favorable flow structures are preserved, with only minor degradation at very large travel distances (such that the wing has passed through several rotations).

Wolfinger and Rockwell [44] expanded on these findings by analyzing a larger aspect ratio $AR = 2$ wing of varying Ro during the start-up process. They found that for low Ro a strong LEV develops during start-up and persists. At high Ro , the LEV forms during start-up but is then shed into the tip vortex after some time. Studies involving variation of aspect ratio [27,29,40,41] have further highlighted the need to understand the degradation of flow structures with increasing radial distance, as well as the surface pressure distributions, and lift and drag at extreme values of Rossby number.

Unresolved Issues

For the case where the radius of gyration of a rotating wing having fixed (low) aspect ratio is systematically varied over a wide range, a number of aspects of the flow physics in relation to the forces acting on the wing have not been fully addressed. It is hypothesized that a number of mechanisms contributing to the vortex physics may be important, but they have not been fully identified or explored in relation to the wide range of values of Rossby number and travel distance of the wing. These physical mechanisms are: transformation of the leading-edge and tip vortices from a laminar to a degraded state, and the location of such breakdown along the span of the wing; spanwise distortion of the leading-edge vortex towards, for example, an archlike vortex; onset of shedding of the leading-edge vortex, as opposed to a stable leading-edge vortex; and the form, trajectory, and degree of coherence of the tip and root vortices downstream of the wing, and the manner in which they either connect or remain unconnected within the near field of the wing.

These features of the flow structure will be intimately related to patterns of instantaneous surface pressure coefficient that determine the overall loading of the wing. The possible occurrence of regions of large suction pressure, as well as regions of positive pressure, as a function of Rossby number and travel distance, and their relation to the flow physics, remains unclarified. Moreover,

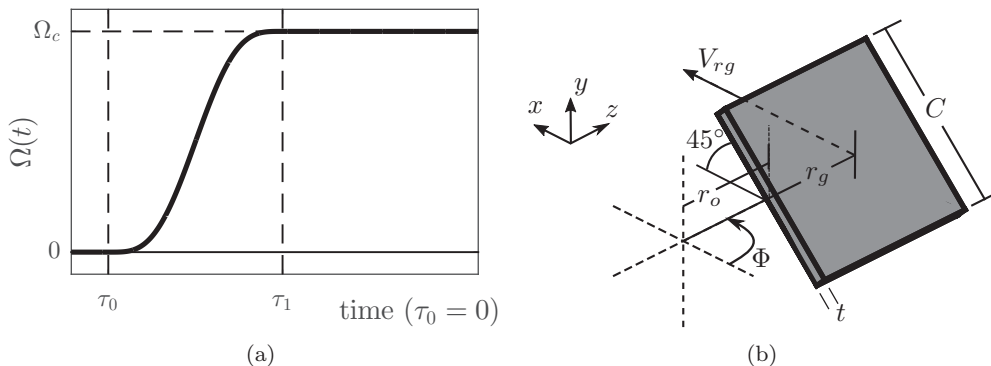


FIG. 1. (a) Velocity profile used for wing motion. (b) Schematic of the “wing.”

the degree to which the value of Rossby number influences the magnitude of the lift coefficient and, furthermore, how it changes the form of the lift coefficient as a function of travel distance, has not been addressed.

II. METHODOLOGY

A. Numerical method

The numerical method used in the present study has been adapted from that of Harbig *et al.* [27] using the commercial code ANSYS CFX version 16.2. The flow over the rotating wing is modeled by the Navier-Stokes equations cast in a noninertial rotating frame of reference along with the continuity constraint

$$\frac{\partial \rho \mathbf{u}}{\partial t} + \nabla \cdot (\rho \mathbf{u} \mathbf{u}) = -\nabla p + \mu \nabla^2 \mathbf{u} - 2\rho(\boldsymbol{\Omega} \times \mathbf{u}) - \rho[\boldsymbol{\Omega} \times (\boldsymbol{\Omega} \times \mathbf{r})] - \rho \dot{\boldsymbol{\Omega}} \times \mathbf{r} \quad (1)$$

and

$$\nabla \cdot \mathbf{u} = 0. \quad (2)$$

Here ρ is the density, \mathbf{u} is the velocity in the rotating frame, p is the pressure, μ is the molecular viscosity, $\boldsymbol{\Omega}$ is the rotational velocity vector, and \mathbf{r} is the position vector. Spatial discretization was carried out using the formally second-order-accurate blend-factor scheme with $\beta = 1$, and a second-order backward Euler scheme was used to integrate forward in time.

B. Geometry and motion

The geometry of the wing is similar to that used by Wolfinger and Rockwell [6] and is shown in Fig. 1(b). A simplified model of a wing was used with rectangular planform, an aspect ratio of unity, and a thickness to chord ratio of 0.08 and is positioned at a geometric angle of attack of 45° and rotated about an axis aligned with the y direction. The aspect ratio of the wing is calculated from the chord length and the span, not including the root cutout,

$$AR = (r_t - r_r)/C, \quad (3)$$

where r_t and r_r are the tip and root radii of the wing.

The wing is initially at rest in a quiescent fluid before being rapidly accelerated to a constant rotational velocity, Ω_c . The imposed angular velocity profile is defined by a piecewise polynomial fit to allow smooth transitions between different phases of the motion (stationary, accelerating, constant velocity, and deceleration). In particular, it produces a motion profile that is continuous up to and

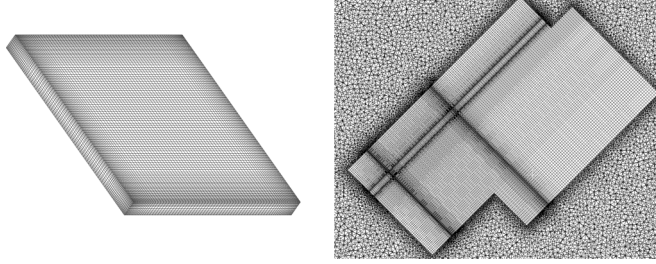


FIG. 2. Mesh used for simulations. Left: The surface mesh that was swept away from the body to create a volume mesh. Right: A slice through the volumetric mesh showing the hexahedral mesh swept into two near-field boxes and a tetrahedral mesh in the far field.

including the 2nd derivative of rotational acceleration. The motion profile is given by

$$\Omega(t) = \begin{cases} (-20(\frac{t}{\tau_1})^7 + 70(\frac{t}{\tau_1})^6 - 84(\frac{t}{\tau_1})^5 + 35(\frac{t}{\tau_1})^4), & t < \tau_1 \\ \Omega_c, & t \geq \tau_1. \end{cases} \quad (4)$$

Here Ω_c is the constant final rotational velocity and τ_1 is the time at which that velocity is first reached. The coefficients of the polynomial were determined by imposing the conditions that $\Omega(0) = 0$, $\Omega(\tau_1) = \Omega_c$ and that higher order derivatives are continuous at $t = 0$ and $t = \tau_1$. This produces the motion profile shown in Fig. 1(a). A value of τ_1 was chosen such that the wing achieves maximum velocity in one chord length of travel, while the value of Ω_c was determined such that $Re = 1400$ based on the constant velocity at the radius of gyration ($V_{rg} = \Omega_c r_g$) and the chord (C).

Initially, the wing was positioned so that the root radius was at $r_o = 0.62C$, producing a Rossby number based on the radius of gyration [33] of $Ro = r_g/C = 1.2$. A parameter sweep was conducted with r_o varied through $0.12C$, $0.37C$, $0.62C$, $0.87C$, $1.12C$, $1.37C$, $1.62C$, $2.62C$, $4.62C$, and $8.62C$, corresponding to Rossby numbers of $r_g/C = 0.7, 0.9, 1.2, 1.4, 1.6, 1.9, 2.1, 3.1, 5.1$, and 9.1 , respectively. This set expands on those used in the experimental study of Wolfinger and Rockwell [6]. An increase in radius of gyration represents a reduction of rotational effects relative to translational effects.

C. Mesh and time step validation

The simulation method is based on that used by Harbig *et al.* [27], although the method of spatial discretization varied. Where Harbig *et al.* [27] used a predominantly tetrahedral mesh with a prismatic inflation layer on the wing, the simpler geometry used in the current study allows for a predominantly hexahedral near-field mesh to be used. The wing surface is divided into rectangular elements, as shown in Fig. 2. This is swept in all directions to create a volume of hexahedral elements in the near field. The far field was discretized with tetrahedral elements, with nodes matching at the interface between hexahedral and tetrahedral elements. Approximately 12 million elements were used in this study (varying slightly with Rossby number) with a biased hexahedral region to increase resolution near the wing corners, where element spacing was $0.0035C$. Mesh independence was verified by comparing predicted forces to those from a mesh of approximately 20 million elements; at $Ro = 1.2$ this resulted in less than a 0.4% difference in mean forces over the last four chord lengths of travel. A time step corresponding to $0.015C$ of wing movement per step was found to be sufficient for convergence; halving the time step produced a variation of less than 0.2% in mean forces.

The computational domain is cylindrical in the same form as Harbig *et al.* [27], with a diameter of 34 wingspans (with the rotation axis at the center) and a height of 44 chord lengths (with the wing positioned centrally in the vertical direction).

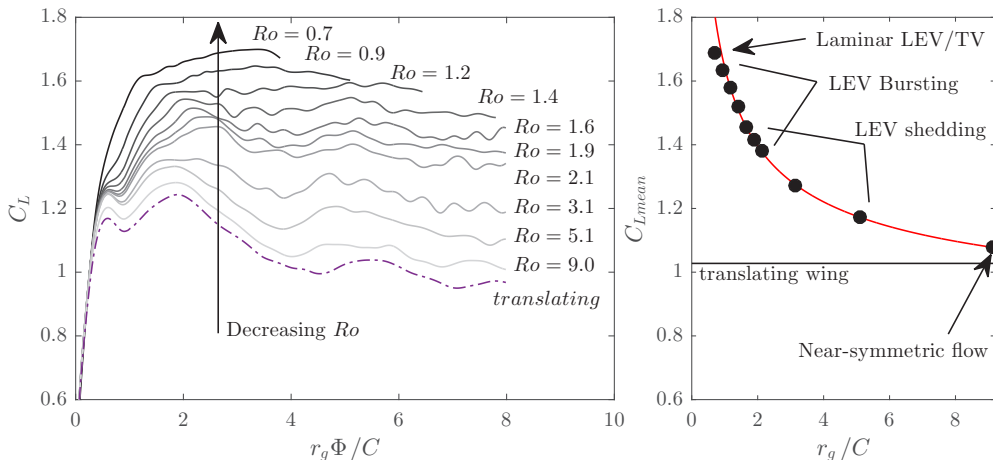


FIG. 3. Lift force coefficient comparisons, with lift force normalized by dynamic pressure at r_g and planform area. Left: Time history for varying r_g/C , plotted over the first eight chord lengths or 330° of travel, whichever occurs first. Right: Mean lift force, with the mean taken between $3 < r_g \Phi / C < 6$ for $Ro \geq 1.2$ and $150^\circ < \Phi < 300^\circ$ for $Ro = 0.7$ and 0.9 .

III. RESULTS

A. Time history of forces

The lift forces, shown in Fig. 3, and the pressure on the upper wing surface in Fig. 4 coincide with features of the velocity field found by Wolfinger and Rockwell [6], with low pressures corresponding to vortical structures, while lift coefficient reduction at high Ro and travel distance correspond to the deterioration of the LEV.

After being near-impulsively accelerated (over one chord length of travel), the forces rise for the first one to two chord lengths of travel, depending on Ro as the flow structure develops. For higher Ro the lift coefficient peaks some time after the acceleration has ended and then decreases, while for the lower Ro the force first stabilizes and then continues to rise throughout the wing's motion until the wing begins to encounter its own wake. The force peak is initially delayed as Ro increases until $Ro \geq 3.1$, where it advances slightly. The initial delay of the force peak appears to be caused by differences in the shedding of the leading-edge start-up vortex. At low Ro this vorticity is shed into the tip vortex soon after the acceleration has ended. However, as Ro increases up to 2.1, the leading-edge starting vortex initially lifts to form an arch and there is a larger separation region associated with the LEV. This allows this start-up structure a longer time to break down and be contained within this region before shedding and merging into the tip vortex. For $Ro \geq 3.1$ the force peak advances in time. This change in regime is due to the feet of the arch-type vortex lifting from the surface of the wing, reducing suction on the upper surface, while a second force peak occurs between $r_g \Phi / C$ of 4 and 5.5 due to this vortex bursting, followed by it being shed and merging into the tip vortex. At the lowest Rossby numbers, $Ro \leq 1.2$, this starting vortex is better maintained so that it does not lift to form an arch structure or breakdown in the same fashion; consequently, there is no force peak and reduction associated with the lifting and shedding of this start-up vortex.

The observation of an *arch vortex* is consistent with the $AR = 2$ results presented in Wolfinger and Rockwell [44], who found experimentally at higher Ro , the starting LEV forms an arch vortex that develops relatively slowly and is then swept into the wake of the wing. The structure of the arch vortex was first defined in the computations of Visbal [45] on a heaving wing; its structure is generic for different wing motions and it has been confirmed experimentally on a heaving wing [46] and on a pitching wing with an inflow [47].

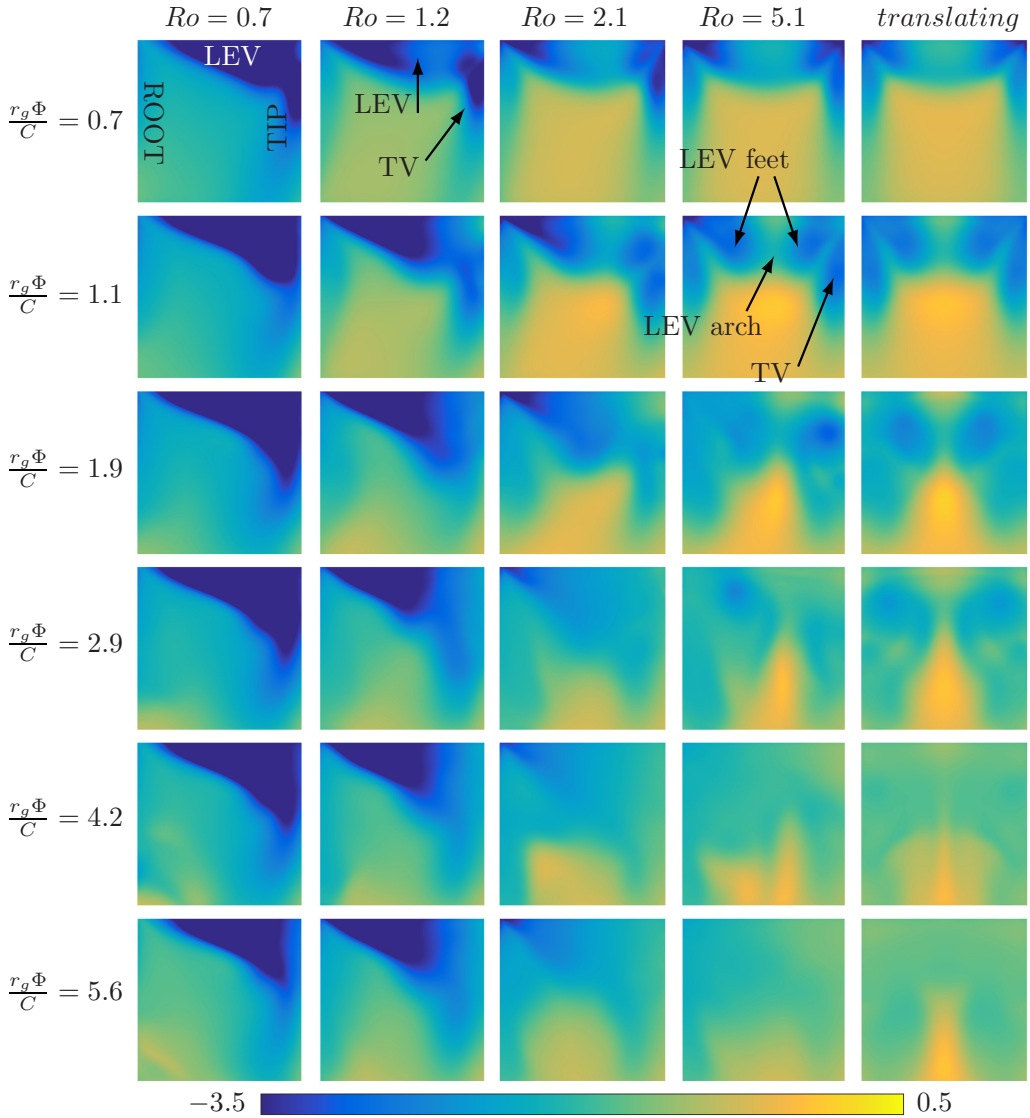


FIG. 4. Instantaneous pressure coefficient on the upper surface of the wing for varying Rossby number and travel distance.

It is noted by Lentink and Dickinson [7] that flying animals typically have a Rossby number based off the tip radius close to 3 (corresponding to $Ro \approx 2.5$ as based on the radius of gyration in the present study). Although aspect ratio also needs to be considered, this would correspond to a region where the leading-edge start-up structures are better retained, creating a higher peak force.

At larger travel distances ($r_g \Phi / C \gtrsim 6$ and/or $\Phi \gtrsim 270^\circ$), the lift force decreases for all cases. For higher Rossby numbers this decrease appears to be due to flow structure degradation, as the system is not capable of retaining stable high-leading-edge vorticity and favorable flow structure development during start-up, as was demonstrated by Wolfinger and Rockwell [6] for $Ro = 5.1$ and for $r_g \Phi / C \gg 10$. For $Ro \leq 1.2$, however, lift decreases because the wing starts to encounter the downwash it generated during start-up beyond Φ of 270° .

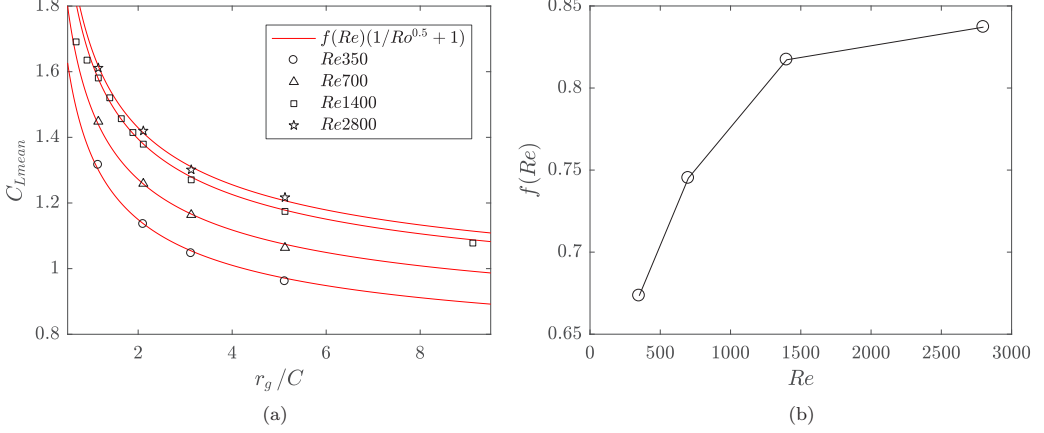


FIG. 5. (a) Variation of mean lift force with both Rossby number and Reynolds number. Mean taken between $3 < r_g \Phi / C < 6$ for $Ro \geq 1.2$ and $150^\circ < \Phi < 300^\circ$ for $Ro = 0.7$ and 0.9 . (b) The Reynolds number function as given in Eq. (7), plotted across the range of Re tested.

Figure 3 (right) shows the variation of mean lift force with Rossby number. In this case, the mean is taken over $3 < r_g \Phi / C < 6$, except in the low-Rossby-number cases of $Ro = 0.7$ and 0.9 , which begin to encounter their shed wake before $r_g \Phi / C = 6$. For $Ro \leq 0.9$ the average is instead taken over $150^\circ < \Phi < 300^\circ$. Figure 3 (right) highlights the flow structure variation that occurs over the range of Ro tested.

Figure 5 presents the variation of mean force expanded to include a limited dataset at $Re = 350, 700, \text{ and } 2800$ in addition to the $Re = 1400$ results already presented. It has been demonstrated by other researchers that in this Reynolds number range there is a general increase in lift force for increasing Reynolds number. Figure 5 shows that the combined effect of Rossby number and Reynolds number can be simplified as a product of a function of the Reynolds number and a function of the Rossby number:

$$C_{Lmean} = f(Re)f(Ro). \quad (5)$$

The Rossby number function is determined by the specific geometry and how the Rossby number is defined (in this case by the radius of gyration). Empirically, for the given dataset it has been found that

$$f(Ro) = \frac{A}{Ro^{0.5}} + B, \quad (6)$$

that is, that the lift force is a function of $1/Ro^{0.5}$. The constants A and B (which are dependent on the specific geometry) in this case are determined to be roughly equal to each other, so that the equation for C_{Lmean} can be expressed as

$$C_{Lmean} = f(Re) \left(\frac{1}{Ro^{0.5}} + 1 \right). \quad (7)$$

The implication is that Rossby and Reynolds number effects on the mean force trends can be determined separately and combined.

It should be noted that the empirical function $f(Ro)$ applies only to the intermediate range of Rossby numbers, as low Ro results deviate from this trend and the asymptote for high Ro implied by the equation is lower than C_{Lmean} for the translating wing case. For low Rossby number this is not unexpected, as the mean force is taken over a reduced period where the force appears to be continuing to rise before the wing encounters its own shed wake at $\Phi \gtrsim 270$. For exceptionally high

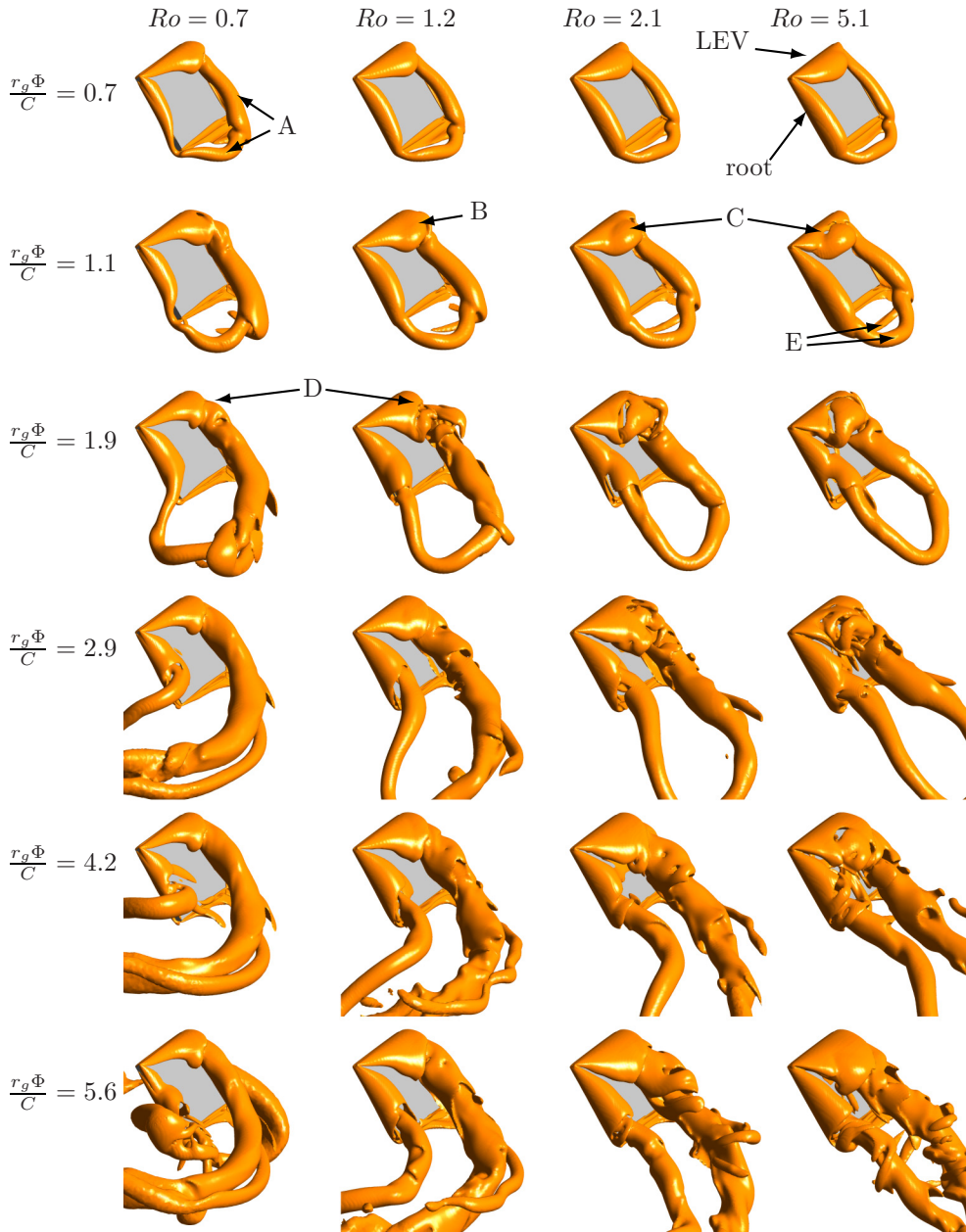


FIG. 6. Development of flow structure as Rossby number and travel distance $r_g \Phi / C$ increase. Isosurfaces plotted at $QC^2 / V_{rg}^2 = 3$.

Ro numbers greater than those tested in the present study, flow likely stabilizes to the translating case rather than continuing to follow the outlined trend.

B. Flow structure development: Pressure and vortex structures

Figure 6 shows the development of flow structures visualized by an isosurface of Q criterion for varying Rossby number, and also the time development within a run for each Rossby number. It

is useful to consider this in conjunction with Fig. 4, which shows the development of the pressure distribution on the upper surface of the wing.

The initial starting vortex structure (travel distance of the wing, $r_g \Phi / C = 0.7$) is similar for all cases, with vortices forming on all edges of the wing. The tip and trailing-edge vortices have already begun lifting away from the surface (A in Fig. 6) while the root and leading-edge vortices are still attached, with the leading-edge vortex being conical in structure. Initially the pressure distributions are similar for each of the rotating-wing cases (Ro from 1.2 to 5.1), with the LEV for lower Ro cases giving a wider region of low pressure near the leading edge.

By $r_g \Phi / C = 1.1$ differences become apparent—the outer portion of the leading-edge vorticity that forms during start-up cannot remain stably attached to the wing, and it starts to lift away from the upper surface for higher Rossby numbers ($\text{Ro} \geq 1.2$). For Ro of 1.2 this occurs only near the tip of the wing (B in Fig. 6); however, the higher Rossby numbers do not sustain the LEV as well and a large portion of the LEV lifts away from the surface as an arch (C in Fig. 6). This is also seen in the surface pressure, where for higher Rossby numbers a gap is present in the region of suction caused by the LEV lifting away with low-pressure regions at the LEV feet (Fig. 4). At $r_g \Phi / C = 1.9$, the lower Rossby number cases have started to shed excess leading-edge vorticity from start-up into the tip vortex (TV), highlighted by D in Fig. 6. The shedding of this excess leading-edge vorticity corresponds to a stabilization of the lift force for the lowest Ro cases (≤ 1.2) and the force peak at higher Ro ($1.4 \leq \text{Ro} \leq 2.1$) observed in Fig. 3.

By this time all Rossby numbers have shed two vortices from the trailing edge highlighted by E in addition to the initial starting vortex. As the flow structures develop in time, the tip vortex and wake structures are increasingly disordered for higher Rossby numbers, in spite of having the same Reynolds number based on chord length.

Even at small travel distances, the translating wing ($\text{Ro} \rightarrow \infty$) shows significant differences from the rotating wings, with larger regions of lower magnitude suction. These correspond to the feet of an arch-type leading-edge vortex as described by Garmann *et al.* [28], which lifts at the center. The regions of suction nearest the tips of the translating wing are the feet of the tip vortices that are lifting from the surface. For the translating wing, the lift force reaches a peak at $r_g \Phi / C = 1.7$, just before the arch-type leading-edge vortex lifts entirely away from the upper surface of the wing. As mentioned previously, this arch vortex is also noted on the $AR = 2$ wing of Wolfinger and Rockwell [44]. The high Ro structures seen in Fig. 6 and the associated force trace resemble the $AR = 1$ translating wing case of Taira and Colonius [48], in spite of the lower Re (300) and angle of attack (30°) of that case.

Figure 7 shows (a) the spanwise velocity and (b) the spanwise vorticity flux (defined as $w_r \omega_z$, where w_r is the spanwise velocity in the relative frame and ω_z is the spanwise vorticity component). These figures are plotted at an instant in time after the forces have stabilized (i.e., after the initial shedding of start-up structures and the arch vortex). Figure 7(a) demonstrates that as the Rossby number increases there is a drop in the spanwise velocity component through the LEV (visualized with isolines of Q criterion). At $\text{Ro} = 1.4$ and 0.50 span the spanwise velocity through the LEV drops rapidly as vortex breakdown is encountered. At $\text{Ro} = 1.6$ and 0.50 span a lower intensity vortex with a positive (though much reduced) spanwise velocity is reestablished, as the core of the LEV begins to reform further from the leading edge and higher off the wing's surface.

Figure 7(b), showing $w_r \omega_z$, gives some indication of the spanwise flow of spanwise-oriented vorticity. This will have some magnitude where spanwise vorticity and spanwise velocity are coincident. It is clear that through the core of the vortex, the spanwise vorticity flux is greater for lower Rossby numbers. The vorticity flux drops to near zero where the LEV bursts for higher Rossby numbers, though recovers a slight positive value closer to the tip as the LEV is reestablished before being drawn in to the tip vortex, though at a much reduced intensity compared to the lower Rossby number cases. Additionally shown is the buildup of negative vorticity flux in the shear-layer region of the LEV. This negative value is due to slight negative velocity as the shear layer is slightly

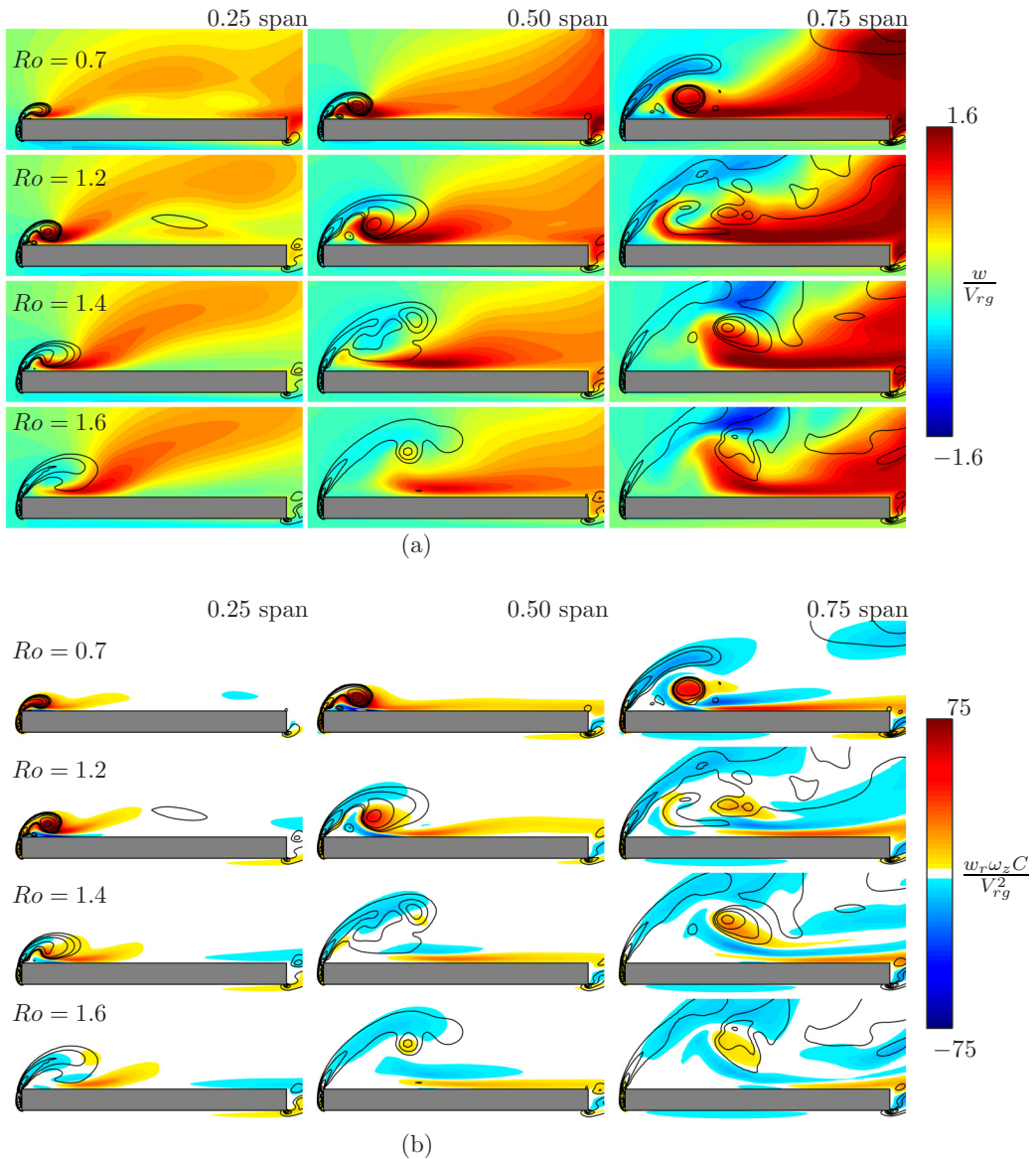


FIG. 7. Spanwise planes taken at 0.25, 0.5, and 0.75 span for varying Ro . (a) Spanwise velocity above the upper surface of the wing. (b) Spanwise vorticity flux $w_r \omega_z$. Plots are overlaid with isolines of Q criterion to visualize the vortex structures.

deflected toward the root of the wing in combination with a very large positive vorticity from the shear layer itself.

Pressure fields on the same spanwise slices are presented in Fig. 8. As would be expected, the pressure is lower in the region of the LEV core where vorticity is highest and the suction at the LEV core reduces as the Rossby number increases. This leads to the pressure distributions already shown previously in Fig. 4. Additionally of note is that the entire separated region and not just the core of the LEV has a much reduced pressure for lower Rossby number.

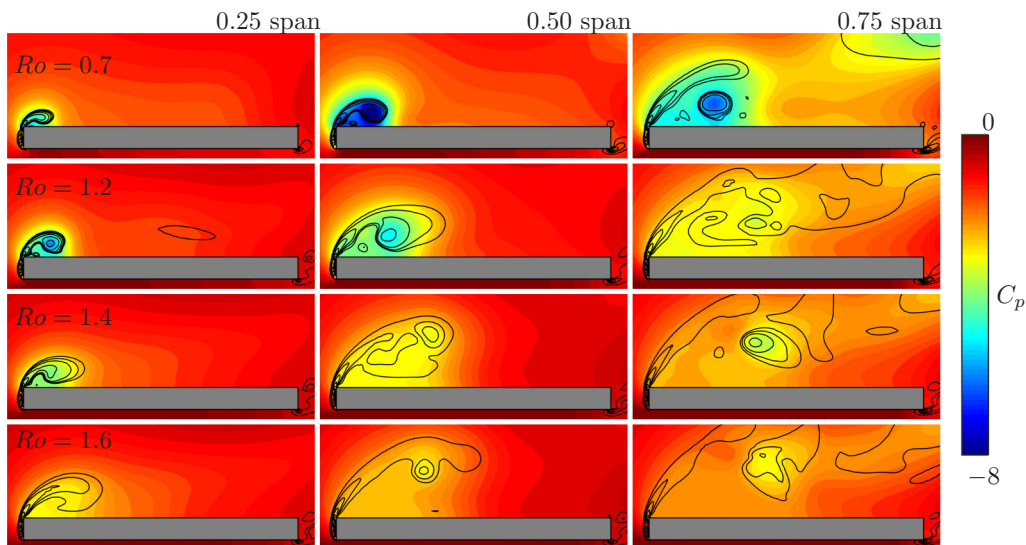


FIG. 8. Spanwise planes taken at 0.25, 0.5, and 0.75 span for varying Ro showing the pressure distribution near the wing.

C. Detailed LEV structure: Particle tracking and planes of Q criterion

To better understand the behavior of the LEV as Ro is varied, particles were released along the leading edge of the wing; these are shown in (Fig. 9) along with planes of Q criterion (Fig. 10). At the lowest $Ro = 0.7$, there is a strong and coherent LEV originating from the root of the wing all the way to the tip, with only a slight deviation at the transition between the LEV and the TV. The particle tracking shows laminar flow throughout the LEV and TV evolution. At $Ro = 1.2$ the same conical LEV is observed; however, there is a sudden expansion around the midspan of the wing characteristic of vortex bursting. The particle trace shows that the flow becomes disordered in the

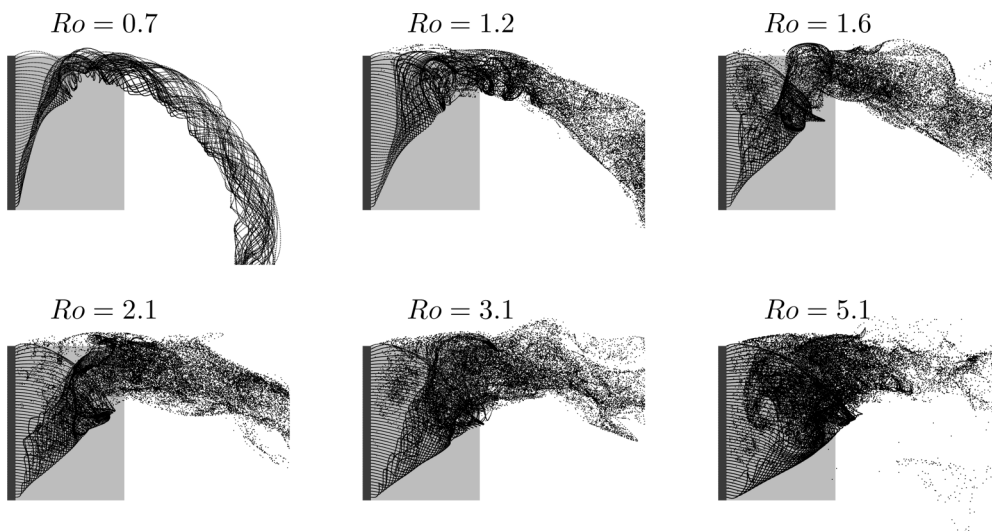


FIG. 9. Particle tracking for a range of Rossby numbers at a travel distance $r_g \Phi / C = 5.5$. See Supplemental Material [51] for a video representation of particle tracking.

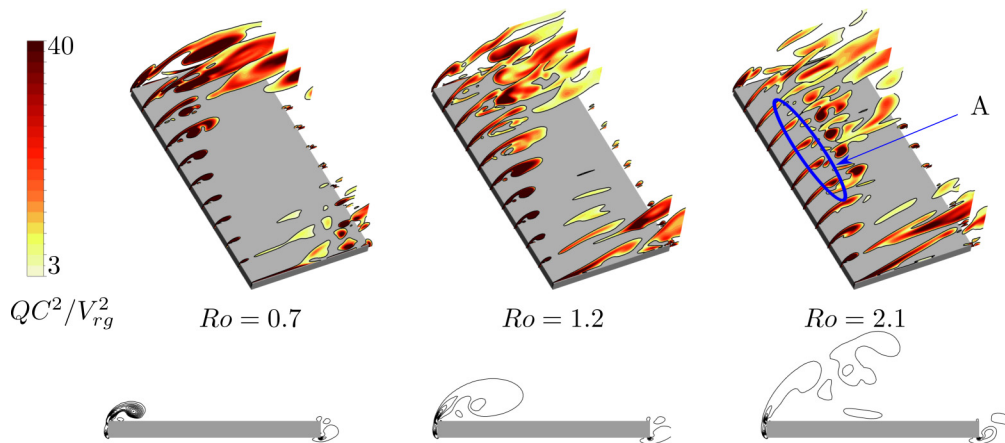


FIG. 10. (top) Slices of Q criterion (bottom) midspan isolines of Q criterion. All results in this figure are given at a rotation angle $\Phi = 230^\circ$. NOTE: To make visualizations clearer, the spanwise direction has been scaled by a factor of 2.

transition between the LEV and the TV. These effects result in a decrease of the LEV core strength near the tip of the wing, as seen in Fig. 10.

For $Ro = 1.6$ and higher the LEV undergoes further changes, with an increasingly larger volume of particles becoming entrained in the larger separated region between the LEV and the upper surface of the wing as the LEV becomes less coherent. In this range of Ro the LEV ceases to remain a stable vortex and transitions to periodic shedding. The region highlighted for $Ro = 2.1$ in Fig. 10(A) shows a buildup of rotational flow fed by the leading-edge shear layer, which sheds into the region of higher Q immediately downstream. The onset time of this LEV shedding varies slightly with Ro , for higher Ro occurring at $r_g \Phi / C \gtrsim 5.5$ after the flow has settled from shedding the excess leading-edge vorticity from start-up. This shedding occurs closer to the tip (>0.3 span for $Ro = 2.1$), while closer to the root the LEV does not shed (<0.3 span), and in the region between shedding and nonshedding regions (~ 0.3 span) the LEV is dominated by shear, making identifying a vortex core difficult.

More general trends as Ro increases are that the LEV is seen to be less intense and forms higher and further back from the leading edge and wing surface, as seen in Fig. 10 for $Ro = 0.7, 1.2,$ and 2.1 . This leads to the lower suction observed in Fig. 4 and an increasingly larger recirculation region that is seen to entrain a larger volume of particles in Fig. 9. This results in the overall reduction in performance, seen through the force history and mean forces presented in Fig. 3. This lifting and weakening of the LEV has been observed nearer the tip of high-aspect-ratio wings in previous aspect-ratio studies [27,29,39–42]. However, this study, along with the experimental flow visualizations of Wolfinger and Rockwell [6], shows a similar trend of degradation, even for low-aspect-ratio wings at higher Rossby numbers. These will directly affect the wing's performance.

IV. VORTEX CORE PARAMETERS

The *health* of the LEV can somewhat be characterized by the flow parameters through the core of the vortex. For this purpose the center of rotation of the LEV is determined using the vortex identification parameter γ_1 , as described by Graftieaux *et al.* [49]. This parameter (γ_1) is a scalar field that is a measure of the rotation around each point in the flow over a defined window. It is given by

$$\gamma_1(P) = \frac{1}{N} \sum_S \frac{(PM \wedge U_M) \cdot z}{\|PM\| \|U_M\|} = \frac{1}{N} \sum_S \sin(\theta_M), \quad (8)$$

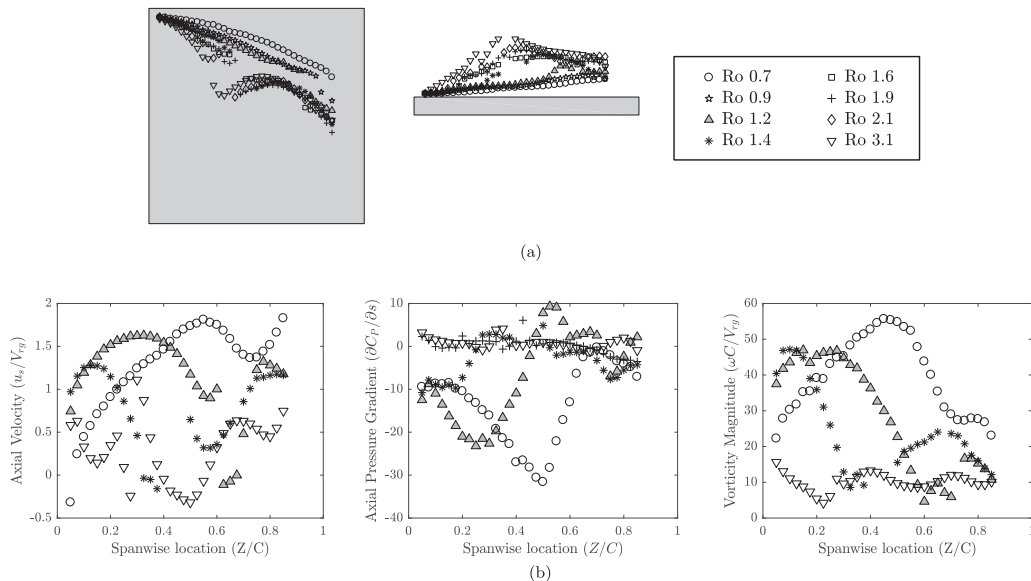


FIG. 11. (a) LEV center of rotation determined from γ_1 (left) as viewed perpendicular to the wing upper surface and (right) viewed front on, perpendicular to the leading edge and parallel to the upper surface. (b) Plots of axial velocity, axial pressure gradient, and vorticity magnitude through the center of rotation of the LEV determined from γ_1 .

where N is the number of points M inside the domain S that surrounds the point of interest P , and U_M is the velocity at the point M .

A peak in γ_1 therefore defines a center of rotation. In this case, the relative frame velocity has been used to determine the center of rotation as the LEV is mostly fixed within the wing's reference frame. The position of the center of rotation as determined by γ_1 is provided in Fig. 11(a). It can be seen that the position of the center of rotation of the LEV initially moves further down and away from the leading edge of the wing as Ro increases. Between $Ro = 1.2$ and $Ro = 1.4$ the LEV breaks down, and the center of rotation is disturbed between 0.3 and 0.4 span before forming again further away from the leading edge at span > 0.4 . The projected frontal view shows that the center of rotation is also further from the surface of the wing.

Figure 11(b) then shows various parameters plotted at the center of rotation: the axial velocity, the axial pressure gradient, and the vorticity magnitude. The axial velocity shows that nearer the root, the higher Ro has higher axial velocity, however, it is short lived, while lower Ro gains and then maintains axial velocity better as the LEV gets closer to the tip. All but the lowest Ro suffer a major drop in axial velocity to near-zero magnitude associated with vortex breakdown. Axial velocity for these cases picks up again further along the span as the LEV is reestablished.

The axial pressure gradient shows similar overall trends, with negative values indicating a favorable pressure gradient. It is seen that the higher Rossby numbers ($Ro \geq 1.9$) do not establish an appreciable favorable pressure gradient through the center of rotation of the LEV, only becoming slightly favorable nearer the tip as the pressure drops, leading into the tip vortex.

The vorticity magnitude through the center of rotation is seen to increase with span until approximately the midspan for the low Ro cases. By comparison, moderate Ro sees only a small increase near the root before dropping, while for high Ro , vorticity magnitude drops immediately from the root of the wing.

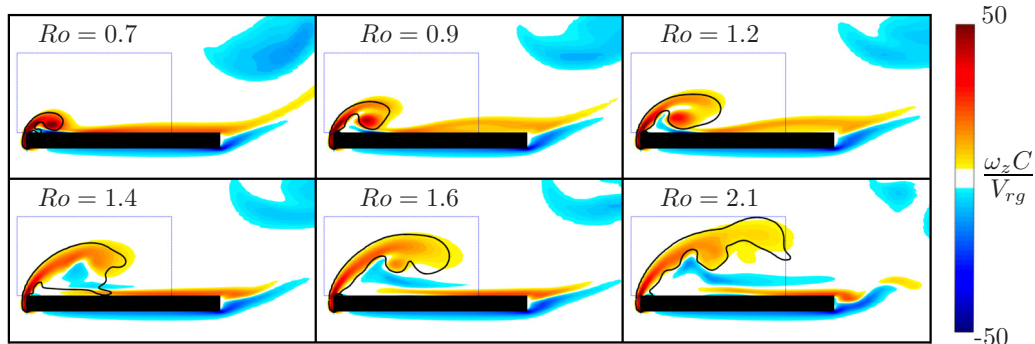


FIG. 12. Midspan spanwise vorticity plot for varying Rossby number. Isoline of $Q = 0$ shown with the black line, region used for the circulation calculation shown by the blue box.

V. SPANWISE CIRCULATION OF LEV

Figure 12 shows midspan plots of spanwise vorticity for a range of Rossby numbers; also plotted are an isoline at $Q = 0$ and a bounding box highlighted in blue. The bounding box shown in this figure was used as the region for calculation of the spanwise circulation of the LEV; the choice of box size is a compromise such that it contains the more dispersed LEV structures for higher Rossby number (requiring a larger box), while avoiding capturing the tip vortex for low Rossby numbers (requiring a smaller box). Figure 12 demonstrates the trend of reduction in strength and lifting of the LEV core for increasing Ro .

Figure 13 shows the spanwise circulation, $\Gamma_z/(V_{rg}C)$, on the upper side of the various wings. The spanwise circulation calculated over the bounding box shown in Fig. 12 is presented in Fig. 13 (top left), described as the “loose” bounding box, while Fig. 13 (middle right) shows the circulation over a rectangular bounding box more tightly fitted to the LEV, sized to capture the region of the LEV where $Q > 0$, as shown in Fig. 12. The isoline of $Q > 0$ was not used in these circulation calculations, as multiple disconnected loops are present in the LEV region when the LEV undergoes breakdown at higher Ro , especially nearer the tip. Both of these plots demonstrate a trend of increasing spanwise circulation in the LEV with span, while the loose box shows lower Ro wings have lower spanwise circulation on the upper surface of the wing nearer the root but higher circulation nearer the tip.

There are various relevant factors that contribute to the behavior. First, from a vorticity generation perspective, the lower Rossby numbers have a lower root speed and higher tip speed, thus generating less circulation from leading-edge separation near the root and more nearer the tip. Second, from a vortex geometry perspective, for low Ro LEV circulation is swept outwards more rapidly and reaches closer to the tip before being reorientated into the wake. The drop off in spanwise circulation at larger spanwise locations is due to vorticity reorientating itself into the wake. These results can be compared with higher-aspect-ratio studies of Phillips *et al.* [42] that showed a general increase in circulation between 0.5 and 0.75 span, and Carr *et al.* [39], which showed reductions in LEV circulation for aspect-ratio 4 compared to aspect-ratio 2 wings when normalizing by the span.

Figure 13 (bottom) shows the spanwise circulation of the LEV integrated across the span of the wing for each Rossby number [i.e., the integral of the curves in Fig. 13(a) plotted against Ro]. When considering the looser box, which better represents the circulation over the entire upper surface of the wing, the total circulation is relatively constant across the range of Ro presented. Considering the tighter box, which better represents the circulation only in the LEV region itself, shows a slight increase in total circulation with increasing Rossby number. These trends highlights that it is not the circulation of the LEV alone which contributes to lift generation, but rather its location, peak intensity, and ability to rapidly reattach the flow that separates from the leading edge.

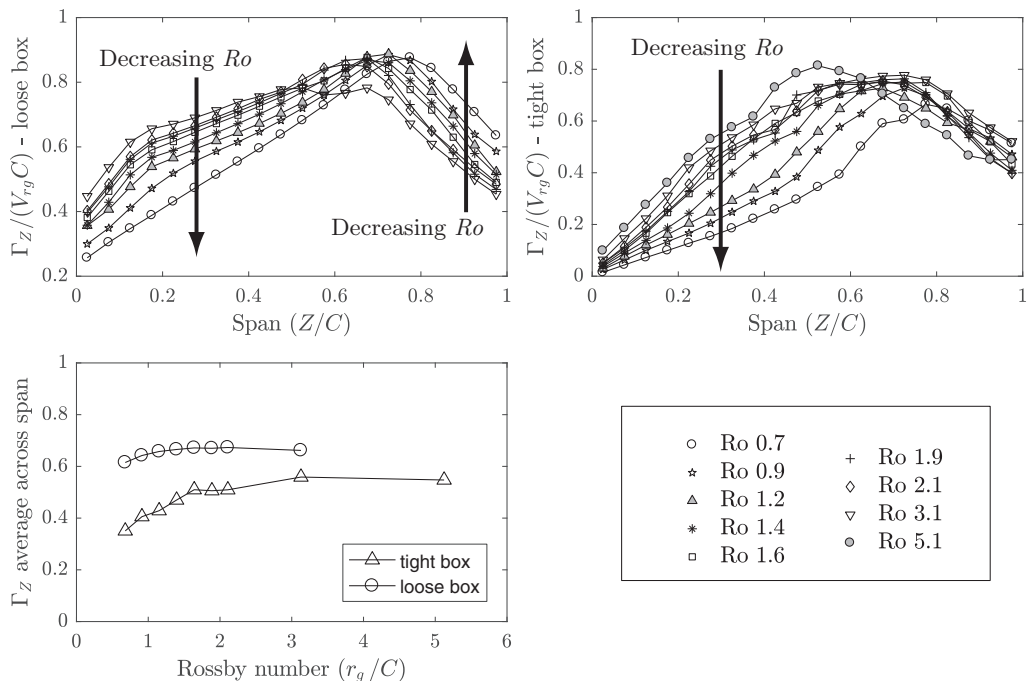


FIG. 13. Spanwise circulation of LEV, $\Gamma_z/(V r_g C)$, (top left) at varying spanwise location from root to tip when calculated over the loose bounding box shown in Fig. 12, (top right) calculated over a tighter rectangular box, sized to only include the LEV where $Q > 0$, and (bottom) the circulation averaged across the span for a range of Ro (r_g/C).

VI. COMPONENTS OF DYNAMIC FORCE

As previously highlighted, the relative contribution of Coriolis and centrifugal forces to the total dynamic force is still not well understood. Although the current study cannot unravel the complexities involved, some trends are highlighted in Figs. 14 and 15.

Figure 15 shows the rotational inertial forces at the point identified as the LEV core (based on the peak in Q criterion on spanwise-oriented planes). This demonstrates the relative direction and magnitude of the Coriolis and centrifugal forces at the vortex core, highlighting their decrease as

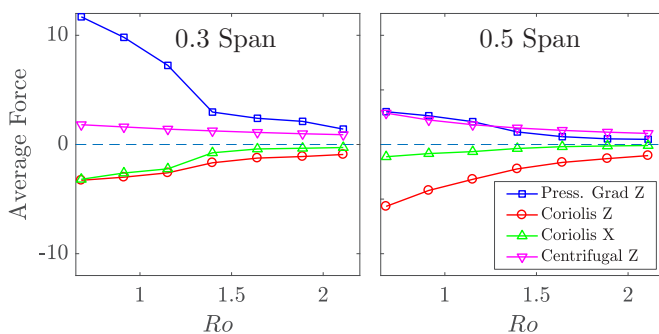


FIG. 14. Pressure gradient, Coriolis, and centrifugal forces averaged across LEV, (left) at 0.3 span and (right) at 0.5 span.

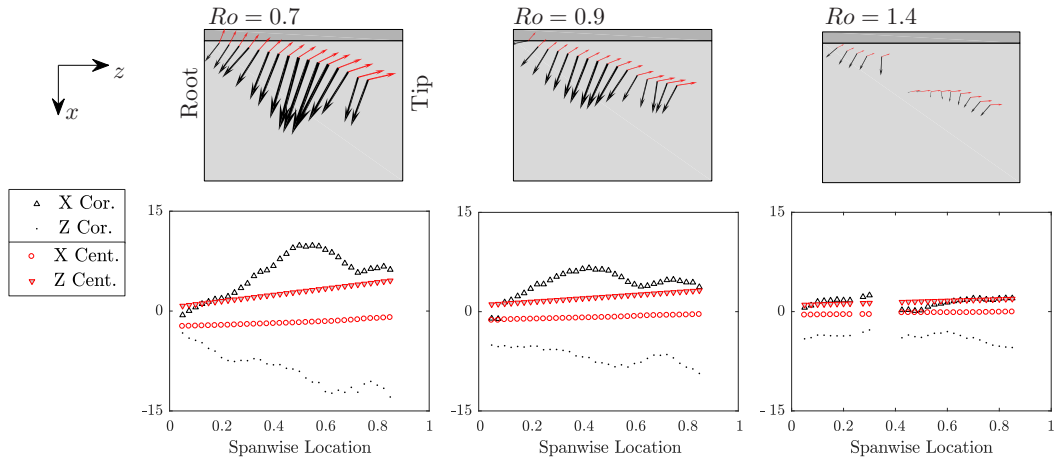


FIG. 15. Centrifugal and Coriolis forces at the leading-edge vortex core (peak Q criterion) for $Ro = 0.7$, 0.9 , and 1.4 .

Rossby number increases. By contrast, the LEV forms closer to the leading edge as these forces decrease.

Figure 14 shows the spanwise components (z direction) of the pressure gradient, Coriolis and centrifugal forces, and also the streamwise (x direction) component of Coriolis force is provided. These force contributions are averaged over the area of the leading-edge vortex bound by $Q > 0$ (as shown in Fig. 12). The graphs are plotted such that positive values are considered favorable to maintain a stable LEV, with forces towards the tip or towards the leading edge being positive, while negative forces are unfavorable, i.e., towards the root or towards the wake. The rotational reference frame forces are expressed in their inertial form.

As the bulk of the spanwise and streamwise velocity in the LEV is towards the tip and towards the wake, it follows that the Coriolis force components must be towards the wake and towards the root, respectively. This is, of course, consistent with the recent study by Limacher *et al.* [37] that identified that Coriolis accelerations limit the spanwise extent of the LEV. While Garmann *et al.* [28] looked at the detailed force component distributions, the aim here was rather to quantify the effects only in an integrated sense.

The change in force component gradients for the 0.3-span case at $Ro = 1.4$ arise from the flow structure changes described previously; the LEV goes from being a singular structure to a less stable time-varying structure. It must be highlighted that Fig. 14 represents averages over the entire LEV; when considered only at the vortex core the spanwise (or axial) pressure gradient is adverse near regions of vortex bursting for $Ro \geq 0.9$. Clearly the results indicate forcing along the wing towards the tip for the pressure gradient and centrifugal components, and towards the root for the Coriolis component, with the overall magnitudes of these competing components decreasing with Ro , as should be expected. Jardin and David [34] highlighted the importance of Coriolis accelerations in generation of lift; however, it is not clear from the present study the mechanism(s) by which this occurs.

The pressure gradient force presented in Fig. 14 is somewhat abstract in that it gives an idea of the relative magnitude of the force in the LEV region, but it is difficult to interpret the actual effect on the LEV. Similarly, the pressure gradient at the vortex core itself has not been presented in Fig. 15, as it will always be positive in radial directions transverse to the vortex axis, and in the direction along the vortex axis, representative of core stability (as presented earlier in Fig. 11). To the end of better understanding the pressure gradient force, presented in Fig. 16 is the pressure plotted on lines which pass through the vortex core. Figure 16 has been broken down into: (left) a line plotted from the leading edge through the vortex core, as this is the direction of force pulling the LEV

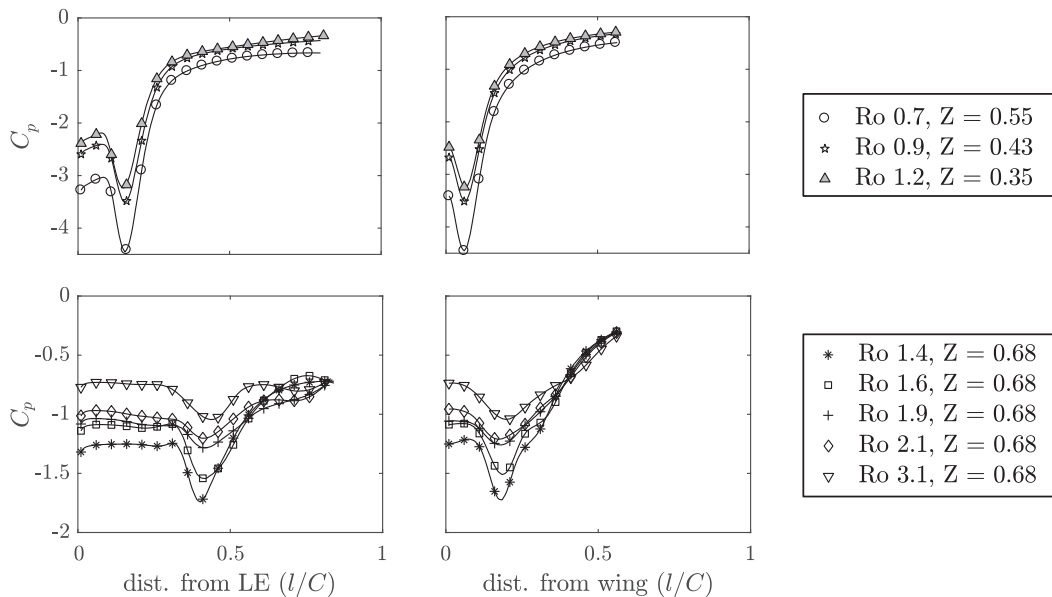


FIG. 16. Pressure plotted on a line starting from the wing surface and passing through the LEV core at the specified spanwise locations, Z . (left) A line starting from the leading-edge corner. (right) A line starting from the upper surface of the wing and projected perpendicular to the wing's surface. (top) Low-Rossby-number cases and (bottom) high-Rossby-number cases after the LEV has broken down.

towards or away from the leading edge; and (right) a line plotted perpendicular to the wing's upper surface, originating at the wing's surface and passing through the LEV core, as this is the direction pulling the LEV towards or away from the wing's surface. Figure 16 has also been broken down by Rossby numbers, with (top) low Rossby numbers before LEV breakdown and (bottom) high Rossby numbers after vortex breakdown and reestablishment. The low Ro number cases have been plotted at different spanwise locations, such that the distance from the LEV to the leading edge is the same, while high Ro number cases are all plotted at the same spanwise location of 0.7 span, as there is little difference in the location of the LEV core for high Ro cases.

The local minima seen in Fig. 16 are at the location of the vortex core, and it can be observed that the suction at the vortex core decreases with increasing Rossby number, as can be observed on two-dimensional planes presented in previously in Fig. 8. However, of interest in Fig. 16 is that the pressure is lower not only at the vortex core itself, but also lower in the region between the vortex and either the wing surface or the leading edge. This is more noticeable in the high-Rossby-number cases on the line plotted from the leading edge (i.e., the bottom left plot in Fig. 16), as there is more space between the LEV core and the wing where the pressure recovery can occur, but is also visible in the low-Rossby-number and high cases. This difference in pressure between either side of the LEV core results in a greater force on the LEV core itself, pulling the core both closer to the wing surface and also closer to the leading edge. This contrasts with the Coriolis force presented in Fig. 15, as the Coriolis force approximately acts in the opposite direction to the force created by a pressure gradient as presented in Fig. 16.

VII. DYNAMIC FORCE DISCUSSION

When examining the effect of Rossby number by itself, three additional major effects can be considered on a rotating wing compared to a purely translating wing affecting the force on a fluid element near the wing: the Coriolis force, the centrifugal force, and a tangential velocity gradient in the spanwise direction. The centrifugal and Coriolis effects are included in the momentum equation

used for simulations [Eq. (1)] to account for being in the wing-stationary noninertial rotating reference frame.

These inertial forces which exist in the wing's reference frame approach zero as the Rossby number approaches infinity (i.e., a translating wing) and are given by

$$\mathbf{F}_{\text{cent}} = -\rho[\boldsymbol{\Omega} \times (\boldsymbol{\Omega} \times \mathbf{r})] \quad (9)$$

for the centrifugal force, and

$$\mathbf{F}_{\text{Cor}} = -2\rho(\boldsymbol{\Omega} \times \mathbf{u}) \quad (10)$$

for the Coriolis force. This demonstrates that the inertial centrifugal force is always acting outwards while Coriolis force is dependent on \mathbf{u} , the local relative frame velocity. If the fluid element is fixed within the wing's reference frame or only in the direction parallel to the rotation axis, the Coriolis force will be zero. For an outward spanwise velocity, the inertial Coriolis force acts to draw the fluid element away from the leading edge and towards the wake (positive x direction), while for a tangential velocity away from the leading edge the Coriolis force is towards the rotation axis (opposing the centrifugal force).

Other than the leading-edge shear layer, which is typically deflected slightly rootwards in the present study, these are the primary flow directions seen at and near the LEV core, such that the Coriolis effect acts mostly to pull the LEV away from the leading edge and towards the root. This result is highlighted in recent studies by Garmann *et al.* [28], Limacher *et al.* [37]. These rotational frame inertial forces—centrifugal and Coriolis—vary with $1/\text{Ro}$, as highlighted by Lentink and Dickinson [7], so long as it is a correct assumption that the relative frame velocities that define the Coriolis force vary with the tangential velocity of the wing.

The other effect of wing rotation that can affect the forces is the tangential velocity gradient in the spanwise direction, as this leads to a gradient in the generated leading-edge vorticity, as it rolls up from the separating shear layer. The difference in the circulation along the wing generates a spanwise pressure gradient. As rotational velocity Ω_C in the presented simulations has been set such that the velocity at the radius of gyration V_{rg} is constant across simulations, it therefore implies the tangential velocity gradient also varies with $1/\text{Ro}$.

Due to each of these rotating effects—the inertial forces and the spanwise tangential velocity gradient—varying with $1/\text{Ro}$, it is not possible to separate the effects by observing a trend in Ro alone.

Lentink and Dickinson [7] presented that it was not the inertial centrifugal and Coriolis forces in and of themselves that stabilize the LEV but rather a reaction to them (i.e., an inward centripetal acceleration reacting against the outward centrifugal force and an outward or upstream acceleration in reaction to the inward or leeward inertial Coriolis force). For the accelerations presented in Lentink and Dickinson [7] to exist, the inertial rotational forces require a reaction, which can be exerted through the wing itself. Lentink and Dickinson [7] presented that this may be through frictional shear forces acting through the fluid onto the wing and was likened to Ekman pumping. Jardin and David [34] presented numerical simulations with and without the Coriolis force to show that the Coriolis force needs to be present to stabilize the LEV, preventing lifting and/or breakdown of the LEV and allowing the wing to produce more lift for a longer period of time.

The current study presents that a greater magnitude inertial Coriolis force pulling the LEV core away from the leading edge exists when the wing is positioned closer to the rotation axis. These cases also have the highest lift force and have the greatest attachment of the LEV core to the leading edge. These lower-Rossby-number cases also have a significantly lower pressure, not only at the vortex core itself, but in the separated region immediately upstream and beneath the LEV core. This demonstrates that as Rossby number decreases, the Coriolis force increases in a manner to push spanwise moving fluid of the LEV away from the leading edge and into the wake; however, the developed pressure distribution in the separated region is associated with pressure differences across the LEV that act to pull it towards the leading edge and the wing surface. This still, however, does not form a complete picture, as it only considers bulk forces on fluid elements in the region of the

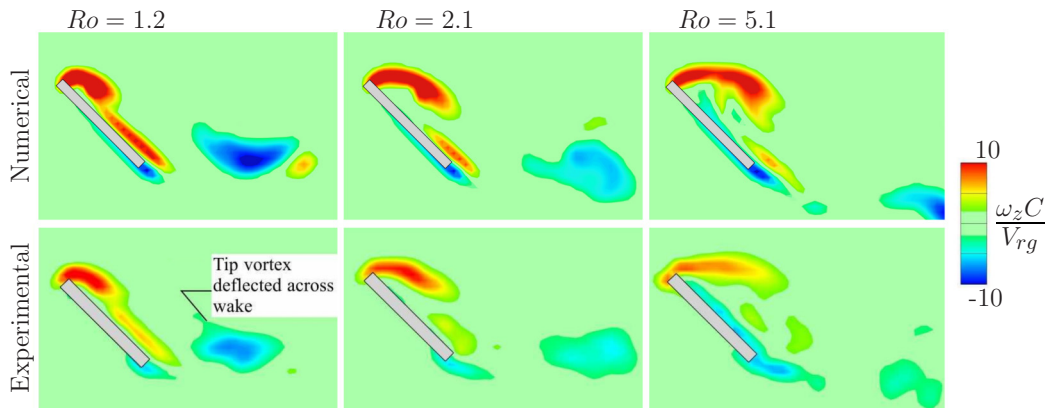


FIG. 17. A comparison of numerical and experimental results. Spanwise planes of spanwise vorticity plotted at the midspan of the wing at a travel distance $r_g \Phi / C = 5.5$ for varying Ro . Experimental results are SPIV results using a nine-image set average, reproduced from Wolfinger [50].

LEV after it has reached a semiequilibrium state, likely generated through nonlinear interactions. In addition, localized effects may contribute to LEV stability in a way that is not immediately obvious or separable from other effects.

VIII. EXPERIMENTAL COMPARISON

Figure 17 shows a comparison of numerical results of the current study alongside experimental results from Wolfinger [50]. For this comparison, the numerical results have been reduced in resolution using a technique similar to that outlined in Garmann and Visbal [29], with results averaged across virtual interrogation windows with overlap to produce a vector spacing the same as that of the SPIV results. Spanwise vorticity (ω_z) was then calculated using central differencing in the same manner as the published experimental results.

The main disparities between the experimental and numerical results are first that the numerical results exhibit a slightly higher magnitude of vorticity in the LEV, the TV, and also the shear layers along the wing's surface. Second, the numerical results show the presence of positive vorticity just behind the negative vorticity of the TV. This positive vorticity is the result of a vortex structure originating from the tip of the wing, fed by the positive vorticity of the shear layer on the top surface of the wing. This shear layer breaks down at higher Ro , resulting in the vortex being less ordered for such cases. There is a small concentration of vorticity in the same location in the experimental results for $Ro = 1.2$; however, it is of much lower strength and it is not clear if this is the same structure. The third discrepancy is in some of the smaller structures not lining up or not being present in the experimental results. This is somewhat to be expected, as the numerical results are an instantaneous snapshot of the flow structure while the experimental results are reconstructed from nine SPIV image sets phase-locked with the wing's motion. The results of the present study have shown that flow structures for higher Ro are unsteady such that in an averaged visualization they may appear as a larger diffused structure rather than small discrete structures if they are not perfectly in phase with the wing's rotation. Importantly, the key finding that the LEV weakens and moves further away from the wing's surface is a consistent feature of both the experimental and numerical results, with the dominant flow structures located in the same positions relative to the wing.

IX. CONCLUSIONS

The results presented herein show that for a wing rotating at constant velocity the performance of the wing degrades as the Rossby number increases. Here, the Rossby number increase is effected

by increasing the radius of gyration. At small Rossby numbers ($Ro \leq 2$) the mean lift coefficient changes rapidly with Ro , but by $Ro \geq 9$ the lift coefficient asymptotically approaches the value for a purely translating wing ($Ro = \infty$).

As the wing starts rotating, its wake structures at different Ro are similar. However, after the acceleration phase the wake structures evolve differently. In particular, the crucial LEV, which remains stable and attached at low Ro , at higher $1.2 \leq Ro \leq 1.6$ bursts, causing it to expand and feed into the tip vortex. Consequently, there is a gradual decline in lift coefficient with time (rotation angle). For $1.6 < Ro \leq 2.1$, the lift force increases during acceleration and then continues to rise to a peak before decreasing; this peak is slightly delayed with increasing Rossby number. This results from the LEV lifting off from the wing, forming an arch that subsequently sheds into the tip vortex. For higher Ro , the drop off after the peak in lift is more rapid with time. This appears to be due to the LEV formed during start-up lifting and breaking down abruptly before being shed into the tip vortex.

The consequences of these different Ro wake evolutions with time on the lift coefficient arise from the formation and evolution of the vortex structures. Their influence on the surface pressures of the wings is clearly seen and explains how the force histories evolve.

An understanding of how the LEV, the primary lift-producing vortex structure, is affected by the balance between Coriolis and inertial forces is clearly important. This work adds to the existing understanding by directly linking the changes in wake structure to the lift forces via the induced pressure fields. It also provides information on the dynamics of the lift generation, which could also be useful to designers of oscillatory rotating-wing devices.

ACKNOWLEDGMENT

A generous computing resource allocation through the National Computational Infrastructure (NCI) under Project No. d71 is gratefully acknowledged.

-
- [1] C. P. Ellington, The novel aerodynamics of insect flight: Applications to micro-air vehicles, *J. Exp. Biol.* **202**, 3439 (1999).
 - [2] S. P. Sane, The aerodynamics of insect flight, *J. Exp. Biol.* **206**, 4191 (2003).
 - [3] M. Dickinson, The effects of wing rotation on unsteady aerodynamic performance at low Reynolds numbers, *J. Exp. Biol.* **192**, 179 (1994).
 - [4] Z. Jane Wang, Dissecting insect flight, *Annu. Rev. Fluid Mech.* **37**, 183 (2005).
 - [5] W. Shyy, H. Aono, S. K. Chimakurthi, P. Trizila, C.-K. Kang, C. E.S. Cesnik, and H. Liu, Recent progress in flapping wing aerodynamics and aeroelasticity, *Prog. Aerosp. Sci.* **46**, 284 (2010).
 - [6] M. Wolfinger and D. Rockwell, Flow structure on a rotating wing: Effect of radius of gyration, *J. Fluid Mech.* **755**, 83 (2014).
 - [7] D. Lentink and M. H. Dickinson, Rotational accelerations stabilize leading edge vortices on revolving fly wings, *J. Exp. Biol.* **212**, 2705 (2009).
 - [8] C. P. Ellington, The aerodynamics of hovering insect flight, I. The quasi-steady analysis, *Philos. Trans. R. Soc., B* **305**, 1 (1984).
 - [9] A. P. Willmott and C. P. Ellington, The mechanics of flight in the hawkmoth *Manduca sexta*, II. Aerodynamic consequences of kinematic and morphological variation, *J. Exp. Biol.* **200**, 2723 (1997).
 - [10] C. P. Ellington, C. van den Berg, A. P. Willmott, and A. L. R. Thomas, Leading-edge vortices in insect flight, *Nature (London)* **384**, 626 (1996).
 - [11] R. J. Bomphrey, N. J. Lawson, G. K. Taylor, and A. L. R. Thomas, Application of digital particle image velocimetry to insect aerodynamics: Measurement of the leading-edge vortex and near wake of a hawkmoth, *Exp. Fluids* **40**, 546 (2006).

- [12] J. M. Birch and M. H. Dickinson, Spanwise flow and the attachment of the leading-edge vortex on insect wings, *Nature (London)* **412**, 729 (2001).
- [13] C. Poelma, W. B. Dickson, and M. H. Dickinson, Time-resolved reconstruction of the full velocity field around a dynamically scaled flapping wing, *Exp. Fluids* **41**, 213 (2006).
- [14] Y. Lu and G. X. Shen, Three-dimensional flow structures and evolution of the leading-edge vortices on a flapping wing, *J. Exp. Biol.* **211**, 1221 (2008).
- [15] M. H. Dickinson, F.-O. Lehmann, and S. P. Sane, Wing rotation and the aerodynamic basis of insect flight, *Science* **284**, 1954 (1999).
- [16] H. Liu, C. P. Ellington, C. Kawachi, C. van den Berg, and A. P. Willmott, A computational fluid dynamic study of hawkmoth hovering, *J. Exp. Biol.* **201**, 461 (1998).
- [17] M. Sun and J. Tang, Lift and power requirements of hovering flight in *Drosophila virilis*, *J. Exp. Biol.* **205**, 2413 (2002).
- [18] H. Aono, F. Liang, and H. Liu, Near- and far-field aerodynamics in insect hovering flight: An integrated computational study, *J. Exp. Biol.* **211**, 239 (2008).
- [19] J. Kweon and H. Choi, Sectional lift coefficient of a flapping wing in hovering motion, *Phys. Fluids* **22**, 071703 (2010).
- [20] T. Jardin, A. Farcy, and L. David, Three-dimensional effects in hovering flapping flight, *J. Fluid Mech.* **702**, 102 (2012).
- [21] J. M. Birch, Force production and flow structure of the leading edge vortex on flapping wings at high and low Reynolds numbers, *J. Exp. Biol.* **207**, 1063 (2004).
- [22] G. Luo and M. Sun, The effects of corrugation and wing planform on the aerodynamic force production of sweeping model insect wings, *Acta Mech. Sin.* **21**, 531 (2005).
- [23] S. A. Ansari, N. Phillips, G. Stabler, P. C. Wilkins, R. Zbikowski, and K. Knowles, Experimental investigation of some aspects of insect-like flapping flight aerodynamics for application to micro air vehicles, *Exp. Fluids* **46**, 777 (2009).
- [24] D. Kim and M. Gharib, Experimental study of three-dimensional vortex structures in translating and rotating plates, *Exp. Fluids* **49**, 329 (2010).
- [25] C. A. Ozen and D. Rockwell, Flow structure on a rotating plate, *Exp. Fluids* **52**, 207 (2011).
- [26] Z. R. Carr, C. Chen, and M. J. Ringuette, Finite-span rotating wings: Three-dimensional vortex formation and variations with aspect ratio, *Exp. Fluids* **54**, 1444 (2013).
- [27] R. R. Harbig, J. Sheridan, and M. C. Thompson, Relationship between aerodynamic forces, flow structures and wing camber for rotating insect wing planforms, *J. Fluid Mech.* **730**, 52 (2013).
- [28] D. J. Garmann, M. R. Visbal, and P. D. Orkwis, Three-dimensional flow structure and aerodynamic loading on a revolving wing, *Phys. Fluids* **25**, 034101 (2013).
- [29] D. J. Garmann and M. R. Visbal, Dynamics of revolving wings for various aspect ratios, *J. Fluid Mech.* **748**, 932 (2014).
- [30] M. Percin and B. W. van Oudheusden, Three-dimensional flow structures and unsteady forces on pitching and surging revolving flat plates, *Exp. Fluids* **56**, 47 (2015).
- [31] M. Bross and D. Rockwell, Flow structure on a simultaneously pitching and rotating wing, *J. Fluid Mech.* **756**, 354 (2014).
- [32] M. Bross and D. Rockwell, Three-dimensional flow structure along simultaneously pitching and rotating wings: Effect of pitch rate, *Exp. Fluids* **56**, 82 (2015).
- [33] D. Lentink and M. H. Dickinson, Biofluiddynamic scaling of flapping, spinning and translating fins and wings, *J. Exp. Biol.* **212**, 2691 (2009).
- [34] T. Jardin and L. David, Coriolis effects enhance lift on revolving wings, *Phys. Rev. E* **91**, 031001 (2015).
- [35] T. Jardin and L. David, Spanwise gradients in flow speed help stabilize leading-edge vortices on revolving wings, *Phys. Rev. E* **90**, 013011 (2014).
- [36] C. J. Wojcik and J. H. J. Buchholz, Vorticity transport in the leading-edge vortex on a rotating blade, *J. Fluid Mech.* **743**, 249 (2014).
- [37] E. Limacher, C. Morton, and D. Wood, On the trajectory of leading-edge vortices under the influence of coriolis acceleration, *J. Fluid Mech.* **800**, R1 (2016).

- [38] J. R. Usherwood and C. P. Ellington, The aerodynamics of revolving wings, I. Model hawkmoth wings, *J. Exp. Biol.* **205**, 1547 (2002).
- [39] Z. R. Carr, A. C. DeVoria, and M. J. Ringuette, Aspect-ratio effects on rotating wings: Circulation and forces, *J. Fluid Mech.* **767**, 497 (2015).
- [40] J.-J. Fu, C. Hefler, H.-H. Qiu, and W. Shyy, Effects of aspect ratio on flapping wing aerodynamics in animal flight, *Acta Mech. Sin.* **30**, 776 (2014).
- [41] J. W. Kruyt, G. F. van Heijst, D. L. Altshuler, and D. Lentink, Power reduction and the radial limit of stall delay in revolving wings of different aspect ratio, *J. R. Soc., Interface* **12**, 20150051 (2015).
- [42] N. Phillips, K. Knowles, and R. J. Bomphrey, The effect of aspect ratio on the leading-edge vortex over an insect-like flapping wing, *Bioinspir. Biomim.* **10**, 056020 (2015).
- [43] K. L. Schlueter, A. R. Jones, K. Granlund, and M. Ol, Effect of root cutout on force coefficients of rotating wings, *AIAA J.* **52**, 1 (2014).
- [44] M. Wolfinger and D. Rockwell, Transformation of flow structure on a rotating wing due to variation of radius of gyration, *Exp. Fluids* **56**, 137 (2015).
- [45] M. R. Visbal, Three-dimensional flow structure on a heaving low-aspect-ratio wing, in *Proceedings of the 49th AIAA Aerospace Sciences Meeting including the New Horizons Forum and Aerospace Exposition, 4–7 January 2011, Orlando, Florida* (AIAA, Reston, VA, 2011), paper AIAA 2011-0219.
- [46] M. Visbal, T. O. Yilmaz, and D. Rockwell, Three-dimensional vortex formation on a heaving low-aspect-ratio wing: Computations and experiments, *J. Fluids Struct.* **38**, 58 (2013).
- [47] T. O. Yilmaz and D. Rockwell, Flow structure on finite-span wings due to pitch-up motion, *J. Fluid Mech.* **691**, 518 (2011).
- [48] K. Taira and T. Colonius, Three-dimensional flows around low-aspect-ratio flat-plate wings at low Reynolds numbers, *J. Fluid Mech.* **623**, 187 (2009).
- [49] L. Graftieaux, M. Michard, and N. Grosjean, Combining PIV, POD, and vortex identification algorithms for the study of unsteady turbulent swirling flows, *Meas. Sci. Technol.* **12**, 1422 (2001).
- [50] M. Wolfinger, Flow structure on a rotating wing: Effect of radius of gyration, Ph.D. thesis, Lehigh University, 2015.
- [51] See Supplemental Material at <http://link.aps.org/supplemental/10.1103/PhysRevFluids.2.064701> for video representation of particle tracking over a range of Rossby numbers.